Solar Energy Materials and Solar Cells 191 (2019) 235–242

Contents lists available at ScienceDirect

Solar Energy Materials and Solar Cells

journal homepage: www.elsevier.com/locate/solmat

CrAlSiN barrier layer to improve the thermal stability of W/CrAlSiN$_x$/CrAlSiO$_y$N$_x$/SiAlO$_x$ solar thermal absorber

A. AL-Rjoub[a,*], L. Rebouta[a], P. Costa[a], L.G. Vieira[b], T.M.R. Miranda[c], N.P. Barradas[d,e], E. Alves[e]

[a] Centre of Physics, University of Minho, Campus de Azurém, 4800-058 Guimarães, Portugal
[b] Centre of Physics, University of Minho, Campus de Gualtar, 4710-057 Braga, Portugal
[c] Centre of Textile Science, and Technology, University of Minho, Campus de Azurém, 4800-058 Guimarães, Portugal
[d] Centro de Ciências e Tecnologias Nucleares, IST, Universidade de Lisboa, Bobadela, Portugal
[e] Instituto de Plasmas e Fusão Nuclear, IST, Universidade de Lisboa, Lisboa, Portugal

ARTICLE INFO

Keywords:
Barrier layer
Optical constants
Thermal stability
CrAlSiN$_x$/CrAlSiO$_y$N$_x$

ABSTRACT

The influence of adding CrAlSiN barrier layer between the back-reflector tungsten (W) and stainless-steel substrate on thermal stability has been investigated. In previous work, after the annealing in vacuum at 600 °C, tungsten diffusion from the back-reflection layer towards the stainless-steel substrate was found. In this study, a barrier layer was added and its influence upon the W diffusion was studied. Several designs of multilayer solar selective absorber for high temperature applications were used to test the thermal and chemical stability and oxidation resistance after vacuum annealing. These samples were characterized by Scanning Electron Microscopy (SEM), Rutherford Backscattering Spectrometry (RBS), X-ray diffraction (XRD), Fourier-transform Infrared Spectroscopy (FTIR) and UV–VIS–NIR spectroscopy. All absorber tandems show good thermal stability after vacuum annealing at 600 °C and the changes in optical constants solar absorptance (α) and thermal emittance (ε) are negligible. In some cases, small changes in the reflectance curves after the first step of annealing were seen. Some changes were found in the oxide layer, due to the incomplete oxidized Si atoms, as confirmed by FTIR analyses. This cannot justify the increase of NIR reflectance observed in the optical stacks after annealing, which can be due to the phase changes of the back-reflector tungsten layer. All layers of stacks are amorphous, except the tungsten layer, which is polycrystalline and shows a columnar growth. The addition of a CrAlSiN$_{P\ =\ 0.11\ Pa}$ barrier layer between tungsten and stainless-steel substrate proved to be a good solution to control the diffusion of W atoms towards the substrate, whereas using higher nitrogen partial pressure in the high and the low absorption layers reduce the diffusion of Cr from those layers to surface.

1. Introduction

The efficiency of solar thermal absorbers does not only depend on the high performance of selectivity, but also strongly depends on the thermal stability, corrosion resistance, oxidation resistance and elemental diffusion between layers [1]. Selectivity is the most crucial and essential condition for high performance and efficient tandems. It means that any solar thermal absorber should have a high absorptance (α) in visible and near infrared (IR) region (wavelength range of 0.3–2.0 μm), and a low thermal emittance in IR region (wavelength range greater than 2.0 μm) [2]. Low thermal emittance in IR region is a vital condition, because the efficiency decreases as the temperature increases due to the thermal radiation loss and the overlapping between the incident solar region and the re-emission thermal spectra [3]. On the other hand, stack's high thermal stability, good diffusion barrier and high oxidation resistance after thermal ageing tests are essential factors for a long lifetime of absorber tandems, resulting in a high competition with other renewable energies, especially for electricity production [4,5]. In most cases, the efficiency of thermal absorber stacks is directly affected by the degradation of the optical properties of the absorber, which is mainly due to diffusion, corrosion resistance and oxidation of the metal back-reflector layer and other metallic components. These issues become more important and present serious challenges at a higher temperature.

Designs based on ceramic-metal composites and those based on transition metal nitrides and oxynitrides are the best-known candidates for solar thermal absorbers, because of their high thermal stability and good oxidation resistance, in addition to adequate results in terms of selectivity. These kinds of absorber stacks almost share the same structural design, that consists of several layers as metal back-reflector

* Corresponding author.
E-mail address: id5811@alunos.uminho.pt (A. AL-Rjoub).

https://doi.org/10.1016/j.solmat.2018.11.023
Received 22 August 2018; Received in revised form 4 October 2018; Accepted 19 November 2018

layer, high and low metal volume fraction for phase interference (absorption layers), covered by oxide antireflection layer [6–11]. However, most designs suffer from poor thermal stability and from elemental diffusion between their layers. For example, Coa et al. reported the diffusion of iron atoms from the stainless-steel into the cermet layer forming a $FeWO_4$ phase [6]. Zhang et al. clearly observed the elemental diffusion of Cr, N and O between the absorbing layer and Al substrate and some microstructure defects appeared [12]. This occurred in a sub-stoichiometric amorphous chromium nitride deposited on an aluminium substrate. Liang et al. confirmed the existence of the element diffusion close to the interface region, in interfaces SiO2/CrOx and CrOx/CrNx, and copper elemental diffusion from substrate throughout all the stacked layers [13]. Kotilainen et al. studied the influence of temperature-induced copper diffusion on the degradation of selective chromium oxynitride solar absorber coating. They recorded a diffusion of copper from the substrate into the coating and through the coating to the surface [14]. In our previous studies [15,16], the Rutherford Backscattering Spectrometry (RBS) and the Time of Flight Elastic Recoil Detection Analysis (TOF-ERDA) methods were very efficient to detect a very small amount of tungsten diffused from the back-reflection layer towards stainless-steel substrate, and some Cr diffused from inner layers, mainly the oxynitride layer, to the anti-reflection oxide layer. Also, a small change in the stainless-steel substrate after air annealing was reported. Wang et al. claimed that they improved the thermal stability of W-Al_2O_3 by adding Ti nano-particles as WTi -Al_2O_3, which revealed that the surface segregation of solute Ti atoms from the parent alloyed nano-particles and their partial oxidation to form protective layer restrain outward diffusion of W element [7].

In most studies reported in the literature, there is a small change in the reflectance curve of the stacks after the first step of annealing in air or vacuum, but for further steps of annealing, it looks more stable. Despite extensive studies on the design and the structure of thermal solar absorber tandems, oxidation resistance and the diffusion process are still difficult to understand.

In our previous studies [15,16], tungsten diffusion from the back-reflection layer towards stainless-steel substrate was found. Although this did not affect the stability of optical properties with the performed annealing, in a long-term time scale, this can contribute to the coating degradation due to the possibility of the formation at the interface of the brittle intermetallic compounds (FeW and Fe_7W_6). In this study, a barrier layer between the stainless-steel substrate and the tungsten back-reflector layer was added and its influence upon the W diffusion was studied. In order to avoid the Cr diffusion from inner layers to the coating surface, as also found in previous studies [15,16], the effect of using higher nitrogen partial pressure in the deposition of nitride layer in the absorber stack is studied in detail. Additionally, the small change after the first annealing step was studied using Fourier-transform Infrared Spectroscopy (FTIR) analyses, in order to understand what is involved in those small changes, which do not happen in subsequent annealing steps.

2. Experimental details

All multi-layer stacks were deposited by dc magnetron sputtering on p-doped Boron Si (100) (used for Scanning Electron Microscopy (SEM)), and polished stainless-steel (AISI304) substrates (used for annealing tests, Rutherford Backscattering Spectrometry (RBS), X-Ray diffraction (XRD) and Fourier-transform Infrared Spectroscopy (FTIR) analyses). The depositions were performed using a substrate holder placed 9 cm above the target and working in static mode. The back-reflection tungsten layers were deposited using a tungsten target (99.99%) with a diameter of 10 cm. A Cr70Al30 at% target was used to deposit $CrAlSiN_x$ layers, where are included the barrier layer and first absorption layer, and $CrAlSiO_yN_x$ layer of the stacks, by adding 9 silicon pellets with a diameter of 10 mm on the target erosion zone. For antireflection $SiAlO_x$ oxide layer, a Si80Al20 at% target was used, with oxygen as a reactive gas. The deposition parameters of different layers were: $P_{Ar} = 0.37$ Pa, current density 6.4 mA/cm^2, pulsed bias of -60 V, f = 90 kHz, room temperature and base pressure 1.2×10^{-4} Pa, except in tungsten layer case, where the current density was 12.7 mA/cm^2. Silicon and stainless-steel substrates were ultrasound cleaned in acetone for 15 min, and ion etched prior the deposition. The detailed simulation with models used for tracing the optical constants of the stacks and their single layers are presented in the previous work [16], and further details about deposition parameters of the coatings are presented in Table 1.

Table 1
Deposition parameters of layers included in different designs (A, B, C and D).

Sample	Layer	Target	Deposition time min: s	Reactive gas and partial pressure (Pa)	Target current density (mA/cm^2)
A (without barrier layer) B (with barrier layer)	CrAlSiN *(only in design B)*	CrAl + 9 Si	2:30	N_2 0.11	6.4
	W	W	2:30	–	12.7
	CrAlSiNx	CrAl + 9 Si	1: 46	N_2 0.05	6.4
	CrAlSiOyNx	CrAl + 9 Si	1: 7	N_2/O_2 (85%/15%) 0.07	6.4
	SiAlOx	SiAl	1:38	O_2 0.06	6.4
C	CrAlSiN	CrAl + 9 Si	2:30	N_2 0.11	6.4
	W	W	2:00	–	12.7
	CrAlSiNx	CrAl + 9Si	2:21	N_2 0.08	6.4
	SiAlOx	SiAl	1: 43	O_2 0.06	6.4
D	CrAlSiN	CrAl + 9 Si	3:00	N_2 0.11	6.4
	W	W	2: 30	–	12.7
	SiAlOx	SiAl	1:30	O_2 0.06	6.4

Samples were subjected to annealing tests in air at 450 °C and in vacuum at 600 °C for 400 h and 300 h, respectively. The vacuum furnace was evacuated to the base pressure of 5.0 mPa and the annealing was performed for several steps. After each step, the vacuum was broken, and the reflectance of samples was measured in order to evaluate the absorptance and the emissivity. Some samples were also analyzed by RBS and FTIR before and after the annealing steps.

RBS measurements were carried out at the CTN/IST Van de Graaff accelerator with detectors placed at 165° to the beam direction. Spectra were collected with a 2 MeV $^4He^+$ beam. Normal incidence was used in the experiments and the obtained data were analyzed with the IBA Data Furnace [17]. Scanning electron microscopy analysis was performed in a NanoSEM-FEI Nova 200 (FEG/SEM) equipment, to determine the coatings' thickness and morphology. The crystalline structure of the absorber coating was studied using X-ray diffraction employing a Bruker AXS Discover D8, operating with $Cu_{K\alpha}$ radiation. X-Ray diffraction measurements were performed using a 3° incidence angle.

The visible and infrared reflectance of samples was measured in the wavelength range of 250–2500 nm, using a Shimadzu PC3101 UV–VIS–NIR scanning spectrophotometer, at an incidence angle of 8° using an integrating sphere attachment and an Al mirror as a reference. The reflectance data were corrected according to theAl -reference reflectance curve. The normal solar absorptance (α_s) was determined from Eq. (1) using experimental spectral reflectance data R(λ) and ASTM AM1.5D solar spectral irradiance, Is(λ), at the wavelength range of 0.3–2.5 μm.

$$\alpha_{sol} = \frac{\int_{0.3\mu m}^{2.5\mu m} I_s(\lambda)[1-R(\lambda)]d\lambda}{\int_{0.3\mu m}^{2.5\mu m} I_s(\lambda)d\lambda} \quad (1)$$

The infrared specular reflectance spectra were measured in the wavelength range of 1.6–16.0 μm at near normal incidence (angle of incidence $\alpha \approx 11°$) with a Fourier Transform Infrared spectrometer Bruker IFS 66 V equipped with a Globar source, a KBr beam-splitter and a DTGS detector with KBr window. The measurements were performed in vacuum at room temperature and spectra were recorded at 4 cm^{-1} resolution with 16 scans. Before the sample measurement, a background reference was performed with an aluminium mirror placed in the same position as the sample. The normal thermal emittance, ε_{th} was calculated as a weighted fraction between emitted radiation and the Planck blackbody distribution at a specific temperature from the equation:

$$\varepsilon_{th} = \frac{\int_{1.6\mu m}^{25\mu m} I_{bb}(\lambda)[1-R(\lambda)]d\lambda}{\int_{1.6\mu m}^{25\mu m} I_{bb}(\lambda)d\lambda} \quad (2)$$

where $I_{bb}(\lambda)$ is the spectral blackbody emissive power and $R(\lambda)$ is the spectral reflectance. The thermal emittance of a polished copper substrate was used to correct data, using a thermal emittance of 3%.

The study of infrared vibrational modes was performed in the wavenumber range of 400–5000 cm^{-1} with the above mentioned FTIR spectrometer and similar conditions, except that *p*-polarized light (polarization parallel to the incidence plane) at oblique-incidence (45°) was used in the reflectance measurements. The spectra were recorded using 128 scans.

3. Results and discussion

3.1. Structure

Four designs (A, B, C and D) were used in this study (Table 1): A is a solar absorber tandem without barrier layer between tungsten and stainless-steel substrate, with structure based on stainless-steel/W/$CrAlSiN_{P\ =\ 0.05\ Pa}$ /$CrAlSiON_{P\ =\ 0.07\ Pa}$ /$SiAlO_{P\ =\ 0.06\ Pa}$, B is the same as A, but with barrier layer included based on $CrAlSiN_{P\ =\ 0.11\ Pa}$, C is a multilayer stack with a nitride layer deposited with higher nitrogen partial pressure and with barrier layer included structure based on stainless-steel/$CrAlSiN_{P=\ 0.11\ Pa}$/W/$CrAlSiN_{P\ =\ 0.08\ Pa}$/$SiAlO_{P=\ 0.06\ Pa}$ and D is a barrier layer with structure based on stainless-steel/$CrAlSiN_{P\ =\ 0.11\ Pa}$ /W/$SiAlO_{P\ =\ 0.06\ Pa}$.

The $CrAlSiN_{P=\ 0.05\ Pa}$ layer used as high absorption layer in our optical stack needs to have enough intrinsic absorption of solar radiation, and for the Cr:Al:Si ratio used cannot be stoichiometric in terms of metal to nitrogen ratio. However, when close to stoichiometry and with enough ion bombardment during deposition, the CrAlSiN layer can have a nanostructure in the form of n-CrAlN/a-SiNx, where CrAlN nanocrystalline grains are embedded in an amorphous SiNx layer [18,19]. This type of nanostructure leads to an improvement of the barrier diffusion properties, as well as, of oxidation resistance and chemical stability, at temperatures as high as 800 °C/900 °C, which was already reported [19–21].

Fig. 1 shows SEM cross-section image of each sample. As observed in the figure, the tungsten layer shows a columnar growth in all designs, whereas the morphology of other layers -including the barrier layer- is not so clear. Thicker single layers with the same coating parameters of tungsten and barrier layers were analyzed by XRD, as shown in Fig. 2.

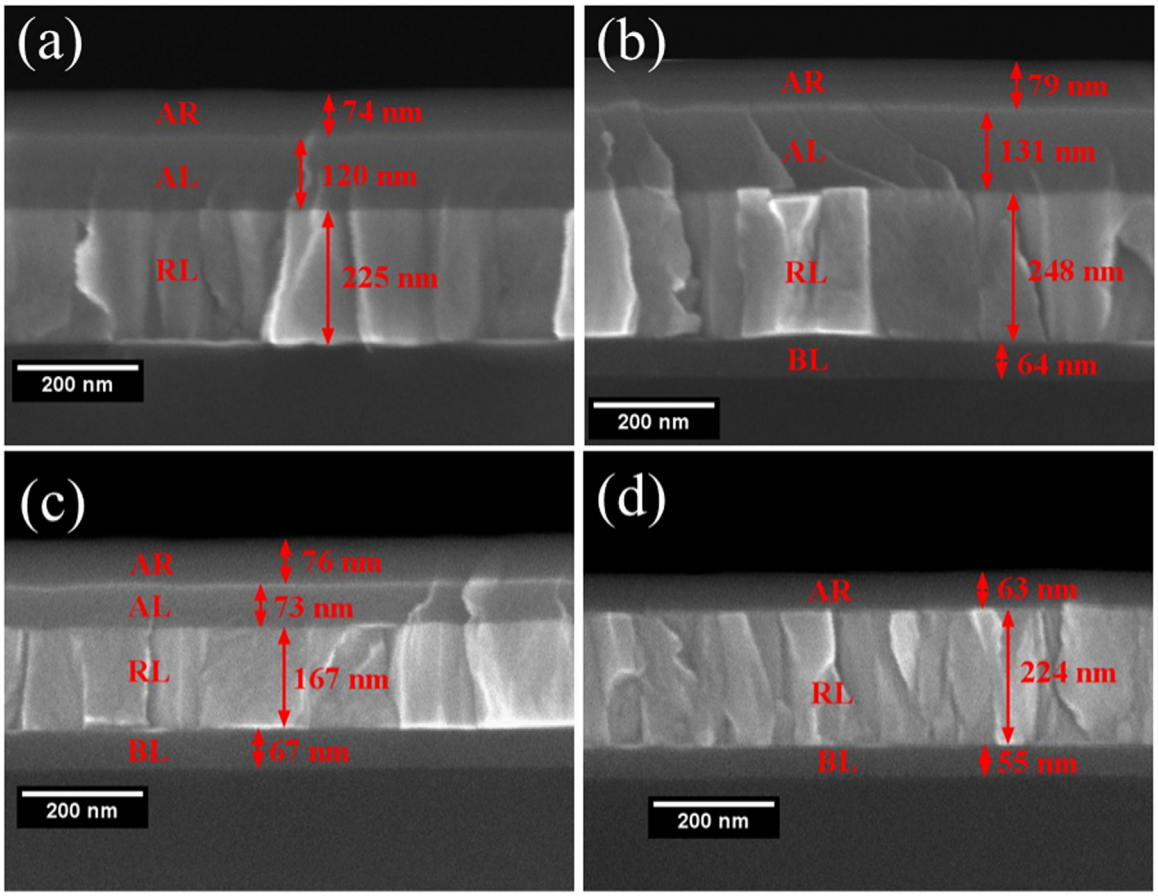

Fig. 1. Cross-sectional SEM images of samples A, B, C and D showing the morphology and the thicknesses. (BL, RL, AL and AR stand for barrier, back-reflector, absorption and antireflection layers respectively). In a) and b) AL in comprised of 2 absorption layers, nitride and oxynitride, whereas in c) is only the nitride layer.

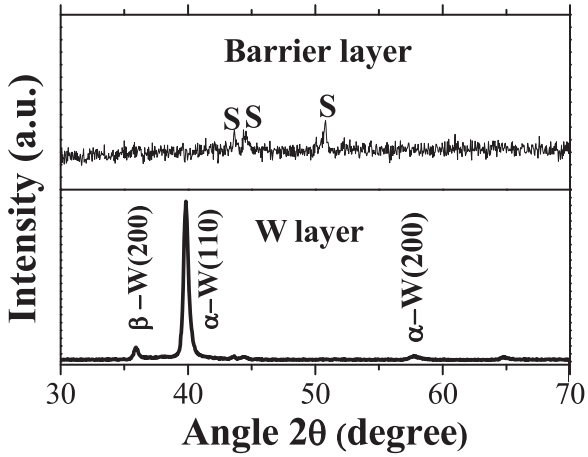

Fig. 2. X-ray diffraction spectra of the single thick of tungsten and barrier layers deposited on stainless-steel.

The XRD pattern of tungsten reveals a combined growth between α- and β- phases, α- being the dominant phase. So, W is polycrystalline with (110) orientation (2θ = 40°). On the other hand, the XRD spectrum of the barrier layer shows no peaks revealing its amorphous structure. The formation of β- phase depends on the partial pressure of oxygen (or base pressure) in the chamber, the film thickness, substrate bias and deposition rate/deposition power [22–24].

3.2. Thermal stability

In previous studies [15,16], thermal stability and elemental diffusion of stacks similar to sample A were studied before and after annealing in air and vacuum at 400 °C and 600 °C, respectively. The stacks revealed an excellent oxidation resistance and layers elemental diffusion, but in the case of vacuum annealing, a diffusion of W atoms towards the stainless-steel substrate and a diffusion of Cr atoms from oxynitride layer towards the surface were recorded. So, we decided to study the effect of adding a barrier layer between the tungsten layer and the substrate (samples B, C, and D), when subjected to a vacuum annealing at 600 °C. In addition, Sample C was also used to study the influence of higher nitrogen partial pressure on the diffusion of Cr from inner layers towards the surface.

Fig. 3 shows the reflectance curves of the four samples measured in the as-deposited state and after vacuum annealing at 600 °C. No noticeable changes are seen in the reflectance curves, solar absorptance (α) and thermal emittance (ε) values for all samples. This implies a very good thermal and oxidation resistance for all stacks. However, small changes in the reflectance curves are observed. In all samples, a small increase of reflectance was found for wavelength higher than 3000 nm. Considering the excellent oxidation resistance and stability of the optical properties with the annealing, these small changes are likely to happen in the back-reflector W layer. To test this, sample D was grown with the antireflection layer deposited directly over the W back-reflector layer, allowing to follow any change in the oxide layer. With the absorption layers and the antireflection layer, FTIR analyses would

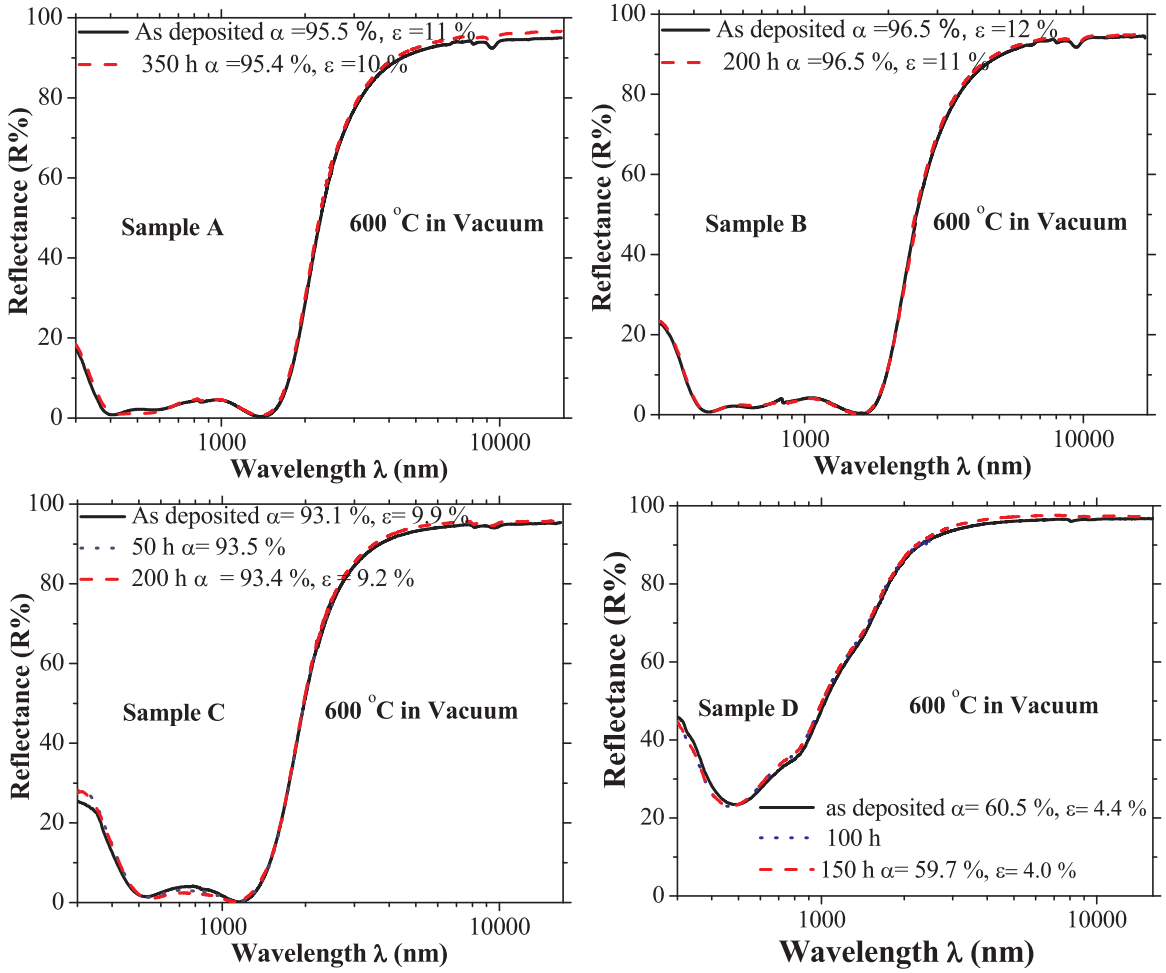

Fig. 3. Reflectance curves of the four samples A, B, C and D, measured in as-deposited state and after vacuum annealing at 600 °C. The emissivity was calculated for 400 °C.

integrate the signals from the three layers. Changes in the first annealing steps followed by steps without significant changes, with very good thermal stability, were reported in our previous studies [9] and by other authors in coatings based on W-Al_2O_3 [25], Mo-SiO_2 [26] and W-SiO_2 [27] cermet composites. The changes were not similar in all cases: in most cases a small increase in reflectance in IR range was observed, but also a small decrease in the reflectance occurred in other cases.

The spectral reflectance shown in Fig. 3 exhibit some changes with the annealing in vacuum. A small increase in the reflectance was found, and this can be due to a W phase transformation during the annealing. A transformation from tungsten β- to α- phase was reported by Antonaia et al. [25] with a small increase in the reflectance for wavelengths higher than 2 μm.

According to O'Keefe et al. [28] differences in the oxygen concentration in the films induce variations in the transformation time and temperature for each sample. The higher the oxygen concentration in the film, the higher the temperature or longer the time required to transform A-15 β-W into bcc α-W. These authors reported a phase transformation at 600 °C, with an annealing time of 1 min, for samples with low oxygen concentration (1–2 at% O). Samples with higher oxygen concentration transformed around 650 °C. This can be the reason the small increase in the reflectance in IR range was not found for all samples. The decrease in the emissivity obtained with the vacuum annealing also supports this conclusion. The β-W phase has higher electrical resistivity than α-W phase [24,28], and the mentioned phase transformation contributes to the resistivity decrease of the W layer and consequent emissivity decrease.

The analyses of infrared bands of sample D show that the oxide layer undergoes small changes after annealing. Fig. 4 shows the experimental oblique-incidence reflectance for *p* polarized light of sample D as-deposited and after vacuum annealing. The lowest frequency part of the spectra amplified in Fig. 4b, shows that after vacuum annealing the main modifications occur in the broad reflectance bands at around 850 cm^{-1} and 1240 cm^{-1}. The later shifts to higher frequencies. and the shape of the band at 850 cm^{-1} is clearly modified. These changes may be due to some local structural rearrangements, e.g., the increment of the oxidation state of some Si atoms. No important absorption is observed in the water absorption spectral region in both cases.

To access and identify the absorbing bands the dielectric function was extracted by simulating the experimental spectra. The modelling was performed by use of Fresnel equations, considering the back medium (tungsten) as a conductor and the oxide layer as a dielectric with optical responses described by the Drude model and the factorized form of the dielectric function [29], respectively. For tungsten we used fixed parameters in the Drude model from the work of Ordal et al. [30]:

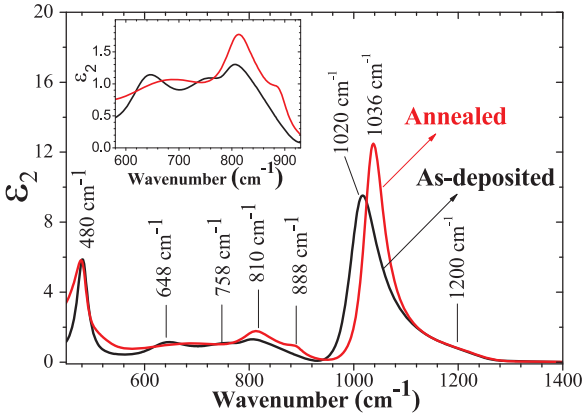

Fig. 5. Imaginary part of the dielectric function of as-deposited and after vacuum annealing at 600 °C of sample D. The inset is an amplification to show the detail of the weaker bands.

plasma frequency - 51,700 cm^{-1}; damping frequency - 467 cm^{-1}. For the oxide layers a high frequency dielectric constant $\varepsilon_\infty = n^2 = 2.31$ (where *n* is the refactive index in the visible spectral range) and the thickness of 63 nm. Fig. 5 shows the imaginary part of the dielectric function (ε_2) for both samples. The ε_2 spectra are roughly similar to the absorption spectrum of amorphous silica. The main three bands with maxima at about 480 cm^{-1}, 810 cm^{-1} and 1020 cm^{-1}/1036 cm^{-1}, can be attributed, respectively, to rocking (R), symmetrical stretching (SS) and asymmetrical stretching (AS) of Si–O bond [31–34]. The other minor bands are identified in Table 2. Notice that the shift of the AS band, well known in the studies of amorphous silica, is usually connected to the increase of stoichiometry in SiO_x [35,36].

Although local structural rearrangements in the oxide layer can give rise to small changes in its high-frequency refractive index, these changes will not induce the reflectance modifications with the annealing shown in Fig. 3 at the wavelength range higher than 2000 nm. For wavelengths higher than 550 nm, the refractive index of the as-deposited oxide layer is 1.52. The simulated reflectance curves of the oxide layer deposited on tungsten varying the refractive index (*n*) of the oxide layer are shown in Fig. 6. The expected variations of *n* are smaller than those simulated in Fig. 6, but with these, it is easier to demonstrate the effect. The simulation shows no changes in reflectance spectra for wavelength greater than 2000 nm due to changes in the refractive index of the oxide layer.

To obtain more information about oxidation resistance after annealing, all samples were studied by XRD and no changes were seen in

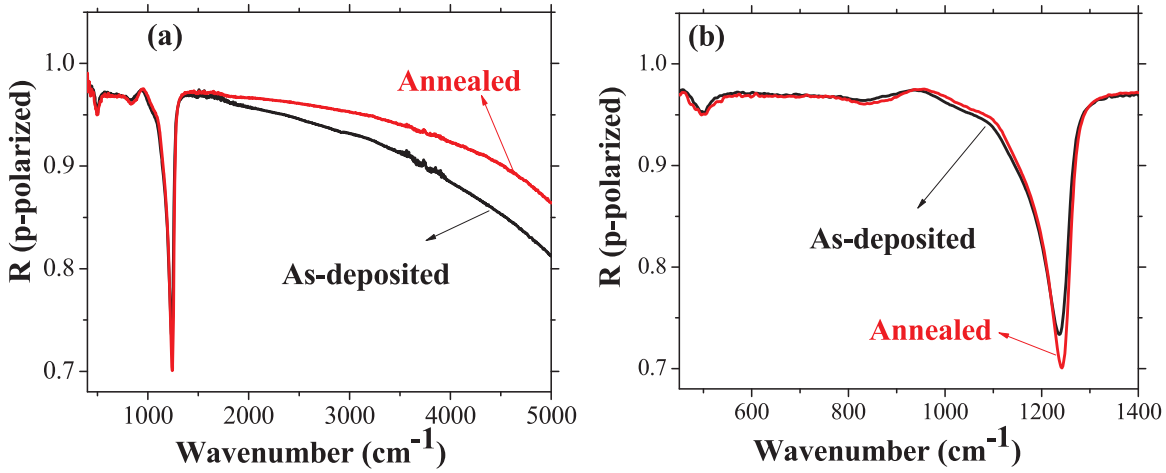

Fig. 4. a) *p*-polarized reflectance spectra (angle of incidence of 45°) of sample D as-deposited and after vacuum annealing at 600 °C. b) Amplification in the spectral range where absorption bands are present.

Table 2
Bands assignment of the FTIR spectra.

Band position (cm^{-1})	Band assignment	Reference
480	Si-O (rocking (R)), or Al-O-Al (bending in AlO_6)	[31–34,37–39]
648	Al-O-Al (bending in AlO_4)	[37–39]
758	T-O-T bending in mixed occupancy tetrahedral (T = Si, Al)	[38,39]
810	Si-O symmetrical stretching (SS)	[38,39]
888	Al − O stretching in AlO_4	[38,39]
1020/1036	Si-O asymmetrical stretching (AS_1)	[31–34,37–39]
1200	Si-O asymmetrical stretching (AS_2)	[31]

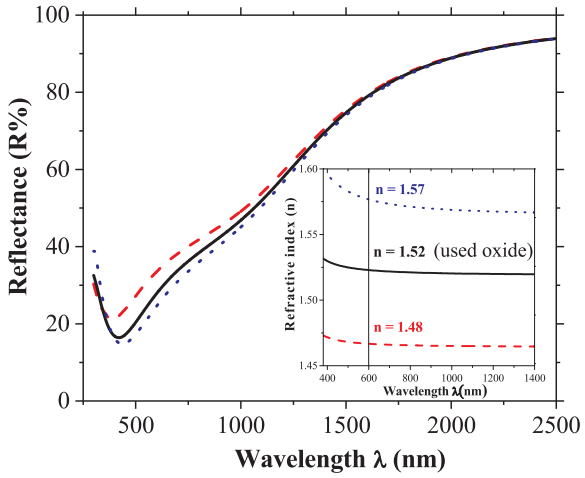

Fig. 6. Simulated reflectance curves of an antireflection oxide layer on tungsten as varying its refractive index (*n*) as shown in the insert.

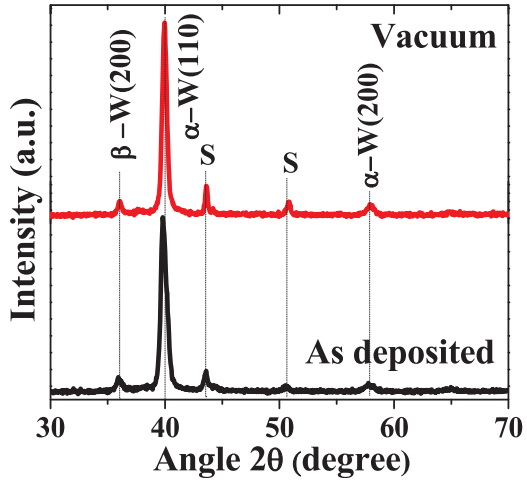

Fig. 7. X-ray diffraction patterns of sample B as deposited and after vacuum annealing at 600 °C.

the XRD spectra after annealing, as shown in Fig. 6 for sample B. No W phase transformation was clearly observed in our samples (see Fig. 7), since XRD peaks associated with both phases continue to have similar intensity before and after annealing. However, the peak located at about 37° showed a small variation of the width and the peak located at 40° revealed a small decrease in the width and a shift to higher angles with a small increase in intensity.

3.3. Elemental diffusion

Elemental diffusion is one of the most important processes of ageing of solar absorber tandems. So, these absorbers can have a long life-time by controlling their elemental diffusion, as well as the oxidation resistance.

In this work, the evaluation of elemental diffusion was studied by RBS. Fig. 8 shows RBS spectra of samples A, B, C and D deposited in the same run, namely as deposited and after vacuum annealing at 600 °C for 200 h. Since the signals from the different elements can overlap, the composition should be determined from the front edges of the elements, which are indicated in figures for better understanding. The relative heights of those front edges are correlated with the relative concentrations of the different elements. The position of the different elements, when located at the surface sample, are indicated in the graph. It is difficult to distinguish between silicon and aluminium because of the small difference of their atomic mass. Sample A, which is a stack without a barrier layer, has a structure similar to the one used in the previous studies [15,16]. The analysis emphasized small differences between as-deposited and annealed sample. The difference between those spectra is in the region of channel numbers 560–580, which is related with the depth profile of W element and corresponds to a tail elongation of the back side of W layer. These differences are in accordance with the diffusion of a small amount of tungsten towards the stainless-steel substrate. The general evaluation shows that no other significant changes occurred after annealing in vacuum. However, in sample B a diffusion barrier layer was added between stainless-steel substrate and tungsten layer to avoid the W diffusion towards the substrate. As seen in the figure, there are no changes in the W depth profile after 200 h of vacuum annealing, which demonstrates the improvement of the stack diffusion without any recorded W atoms diffused towards the stainless-steel substrate. To make sure that the barrier layer works as expected, the barrier layer was also included in samples C and D and the same results were obtained. So, the barrier layer is very effective in preventing the diffusion. In the case of sample C, the stack is composed of the barrier layer, tungsten layer, nitride absorbing layer, which was deposited with higher nitrogen partial pressure, and antireflection oxide layer. This sample was used to study both diffusion cases: Cr towards the surface and W towards the substrate. In both cases, the design shows excellent thermal stability and no diffused elements between layers were recorded. Thus, using higher nitrogen partial pressure in nitride and oxynitride layers can control the diffusion of Cr atoms towards surface because the resulting films are stoichiometric and more stable.

So, increasing of N_2 partial pressure during deposition with best choice of Cr, Al and Si composition decreases the number of Cr at metallic oxidation state and promotes the SiNx segregation [19], improving the oxidation resistance and barrier diffusion properties [18,20], which contributes for the W diffusion reduction [19,21]. One of the advantages is that it is possible to use the same target to deposit the barrier layer, as well as, the nitride/oxynitride absorption layers.

4. Conclusions

Several absorbers with different designs were used to study the thermal stability, oxidation resistance and elemental diffusion between stacks layers. All absorbers show an excellent resistance against oxidation and thermal stability after annealing in vacuum at 600 °C for 200 h. The changes in optical constants solar absorptance (α) and thermal emittance (ε) are negligible, and XRD spectra of all samples are very similar before and after annealing. In some cases, small changes in the reflectance curves after the first step of annealing were seen. The increase in reflectance in IR wavelength range ($\lambda > 3000$ nm) is due to the phase changes of the back-reflector tungsten layer, which also contributes to a decrease in the emissivity after the vacuum annealing. Incomplete oxidized Si as confirmed by FTIR analyses can eventually

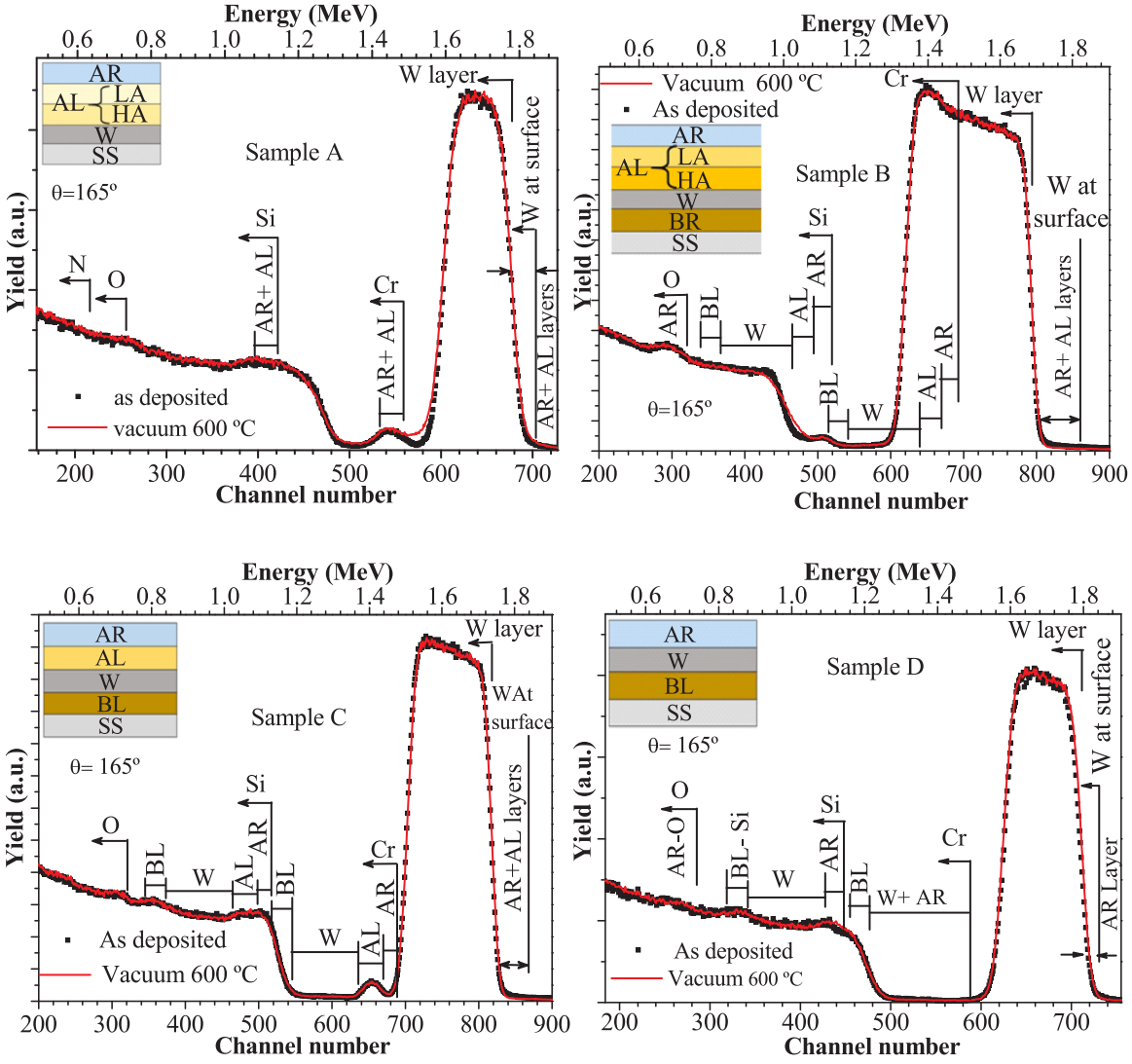

Fig. 8. RBS spectra of the samples A, B, C and D as deposited and after vacuum annealing at 600 °C for 200 h.

introduce small changes in reflectance curves of the stack for wavelengths lower than 1500 nm. All layers of stacks are amorphous, except the tungsten layer, which is polycrystalline and shows a columnar growth. Adding a $CrAlSiN_{P=\ 0.11\ Pa}$ barrier layer between the tungsten and the stainless-steel substrate controls the diffusion of W atoms towards the substrate, whereas using higher nitrogen pressure in HA, LA layers reduces the diffusion of Cr from those layers to the surface.

Acknowledgments

The authors acknowledge the support of FCT in the framework of the Strategic Funding UID/FIS/04650/2013 and the financial support of FCT, POCI and PORL operational programs through the project POCI-01-0145-FEDER-016907 (PTDC/CTM-ENE/2882/2014), co-financed by European community fund FEDER.

References

[1] H. Wang, V. Prasad Sivan, A. Mitchell, G. Rosengarten, P. Phelan, L. Wang, Highly efficient selective metamaterial absorber for high-temperature solar thermal energy harvesting, Sol. Energy Mater. Sol. Cells 137 (2015) 235–242.
[2] C.E. Kennedy, Review of mid-to high-temperature solar selective absorber materials, Natl. Renew. Energy Lab. (2002).
[3] S.A. Cho, R. Fookes, C.A. Garris, Efficiency of ceramic absorber coatings for solar-thermal conversion, Ceram. Int. 7 (1981) 8–12.
[4] IRENA, Renewable energy technologies cost analysis series: concentrating solar power, Compr. Renew. Energy 3 (2012) 595–636.
[5] L. Rebouta, A. Sousa, M. Andritschky, F. Cerqueira, C.J. Tavares, P. Santilli, K. Pischow, Solar selective absorbing coatings based on AlSiN/AlSiON/AlSiOy layers, Appl. Surf. Sci. 356 (2015) 203–212.
[6] F. Cao, D. Kraemer, T. Sun, Y. Lan, G. Chen, Z. Ren, Enhanced thermal stability of W-Ni-Al2O3 cermet-based spectrally selective solar absorbers with tungsten infrared reflectors, Adv. Energy Mater. 5 (2015).
[7] X. Wang, J. Gao, H. Hu, H. Zhang, L. Liang, K. Javaid, High-temperature tolerance in WTi-Al2O3 cermet-based solar selective absorbing coatings with low thermal emissivity, Nano Energy 37 (2017) 232–241.
[8] L. Rebouta, A. Sousa, P. Capela, M. Andritschky, P. Santilli, A. Matilainen, K. Pischow, N.P. Barradas, E. Alves, Solar selective absorbers based on Al2O3:W cermets and AlSiN/AlSiON layers, Sol. Energy Mater. Sol. Cells 137 (2015) 93–100.
[9] D. Dias, L. Rebouta, P. Costa, A. AL-Rjoub, M. Benelmeki, C.J. Tavares, N.P. Barradas, E. Alves, P. Santilli, K. Pischow, Optical and structural analysis of solar selective absorbing coatings based on AlSiOx:W cermets, Sol. Energy 150 (2017) 335–344.
[10] A. Dan, K. Chattopadhyay, H.C. Barshilia, B. Basu, Angular solar absorptance and thermal stability of W/WAlN/WAlON/Al2O3-based solar selective absorber coating, Appl. Therm. Eng. 109 (2016) 997–1002.
[11] A. AL-Rjoub, L. Rebouta, P. Costa, L.G. Vieira, Multi-layer solar selective absorber coatings based on W/WSiAlN x/WSiAlOyNx/SiAlOx for high temperature applications, Sol. Energy Mater. Sol. Cells 186 (2018) 300–308.
[12] Z. Ke, D. Miao, H. Lei, M. Jianping, W. Jining, L. Xiaopeng, D. Zhejun, M. Jie, Z. Bo, Thermal stability test and ageing mechanisms study of different solar selective absorbing coatings, Surf. Coat. Technol. 323 (2017) 65–71.
[13] L. Wu, J. Gao, Z. Liu, L. Liang, F. Xia, H. Cao, Thermal aging characteristics of CrNxOy solar selective absorber coating for flat plate solar thermal collector applications, Sol. Energy Mater. Sol. Cells 114 (2013) 186–191.
[14] M. Kotilainen, M. Honkanen, K. Mizohata, P. Vuoristo, Influence of temperature-induced copper diffusion on degradation of selective chromium oxy-nitride solar

absorber coatings, Sol. Energy Mater. Sol. Cells 145 (2016) 323–332.
[15] A. AL-Rjoub, P. Costa, L. Rebouta, I. Bogdanovi, K. Arstila, N.P. Barradas, A study of solar thermal absorber stack based on CrAlSiNx/CrAlSiNx/Oy structure by ion beams, Nucl. Inst. Methods Phys. Res. B (2018).
[16] A. AL-Rjoub, L. Rebouta, P. Costa, N.P. Barradas, E. Alves, P.J. Ferreira, K. Abderra, A. Matilainen, K. Pischow, A design of selective solar absorber for high temperature applications, Sol. Energy 172 (2018) 177–183.
[17] N.P. Barradas, C. Jeynes, R.P. Webb, U. Kreissig, R. Grötzschel, Unambiguous automatic evaluation of multiple ion beam analysis data with simulated annealing, Nucl. Instrum. Methods Phys. Res. B. 149 (1999) 233–237.
[18] T. Polcar, A. Cavaleiro, High-temperature tribological properties of CrAlN, CrAlSiN and AlCrSiN coatings, Surf. Coat. Technol. 206 (2011) 1244–1251.
[19] S. Veprek, R.F. Zhang, M.G.J. Veprek-Heijman, S.H. Sheng, A.S. Argon, Superhard nanocomposites: origin of hardness enhancement, properties and applications, Surf. Coat. Technol. 204 (2010) 1898–1906.
[20] D.B. Lee, T.D. Nguyen, S.K. Kim, Air-oxidation of nano-multilayered CrAlSiN thin films between 800 and 1000 °C, Surf. Coat. Technol. 203 (2009) 1199–1204.
[21] K. Bobzin, N. Bagcivan, P. Immich, S. Bolz, R. Cremer, T. Leyendecker, Mechanical properties and oxidation behaviour of (Al,Cr)N and (Al,Cr,Si)N coatings for cutting tools deposited by HPPMS, Thin Solid Films 517 (2008) 1251–1256.
[22] Y.G. Shen, Y.W. Mai, Influences of oxygen on the formation and stability of A15 B-W thin films, Mater. Sci. Eng. A 284 (2006) 176–183.
[23] I.A. Weerasekera, S.I. Shah, D.V. Baxter, K.M. Unruh, Structure and stability of sputter deposited beta-tungsten thin films, Appl. Phys. Lett. 64 (1994) 3231–3233.
[24] G.S. Chen, L.C. Yang, H.S. Tian, C.S. Hsu, Evaluating substrate bias on the phase-forming behavior of tungsten thin films deposited by diode and ionized magnetron sputtering, Thin Solid Films 484 (2005) 83–89.
[25] A. Antonaia, A. Castaldo, M.L. Addonizio, S. Esposito, Stability of W-Al2O3 cermet based solar coating for receiver tube operating at high temperature, Sol. Energy Mater. Sol. Cells 94 (2010) 1604–1611.
[26] J. Wang, B. Wei, Q. Wei, D. Li, Optical property and thermal stability of Mo/Mo-SiO2/SiO2 solar-selective coating prepared by magnetron sputtering, Phys. Status Solidi Appl. Mater. Sci. 208 (2011) 664–667.
[27] E. Wäckelgard, A. Mattsson, R. Bartali, R. Gerosa, G. Gottardi, F. Gustavsson, N. Laidani, V. Micheli, D. Primetzhofer, B. Rivolta, Development of W-SiO2 and Nb-TiO2 solar absorber coatings for combined heat and power systems at intermediate operation temperatures, Sol. Energy Mater. Sol. Cells 133 (2015) 180–193.
[28] M.J. O'Keefe, J.T. Grant, Phase transformation of sputter deposited tungsten thin films with A-15 structure, J. Appl. Phys. 79 (1996) 9134–9141.
[29] D.W. Berreman, F.C. Unterwald, Adjusting poles and zeros of dielectric dispersion to fit reststrahlen of PrCl3 and LaCl3, Phys. Rev. 174 (1968).
[30] M.A. Ordal, L.L. Long, R.J. Bell, S.E. Bell, R.R. Bell, R.W. Alexander, C.A. Ward, Optical properties of the metals Al, Co, Cu, Au, Fe, Pb, Ni, Pd, Pt, Ag, Ti, and W in the infrared and far infrared, Appl. Opt. 22 (1983) 1099.
[31] C.T. Kirk, Quantitative analysis of the effect of disorder-induced mode coupling on infrared absorption in silica, Phys. Rev. B 38 (1988).
[32] L. Stoch, M. Sroda, Infrared spectroscopy in the investigation of oxide glasses structure, J. Mol. Struct. 512–511 (1999) 77–84.
[33] J.A. Luna-López, G. García-Salgado, T. Díaz-Becerril, J.C. López, D.E. Vázquez-Valerdi, H. Juárez-Santiesteban, E. Rosendo-Andrés, A. Coyopol, FTIR, AFM and PL properties of thin SiOxfilms deposited by HFCVD, Mater. Sci. Eng. B 174 (2010) 88–92.
[34] R. Al-Oweini, H. El-Rassy, Synthesis and characterization by FTIR spectroscopy of silica aerogels prepared using several Si(OR)4 and R″Si(OR′)3 precursors, J. Mol. Struct. 919 (2009) 140–145.
[35] A. Lehmann, L. Schumann, K. Hubner, Optical phonons in amorphous silicon oxides (II), Phys. Status Solidi B 121 (1984) 505–511.
[36] R. Salh, A. Von Czarnowski, M.V. Zamoryanskaya, E.V. Kolesnikova, H.J. Fitting, Cathodoluminescence of SiOx under-stoichiometric silica layers, Phys. Status Solidi A 203 (2006) 2049–2057.
[37] D.I. Voll, C.H. Lengauer, A.N. Beran, H.A. Schneider, Infrared band assignment and structural refinement of Al-Si, Al-Ge, and Ga-Ge mullites, Eur. J. Miner. 13 (2001) 591–604.
[38] J.-Ch Buhl, Crystallization of hydrosodalite Na6[AlSiO4]6(H2O)8 and tetra-hydroborate sodalite Na8[AlSiO4]6(BH4)2 inside the openings of wafer-thin steel mesh, Adv. Chem. Eng. Sci. 7 (2017) 277–290.
[39] D. Voll, P. Angerer, A. Beran, H. Schneider, A new assignment of IR vibrational modes in mullite, Vib. Spectrosc. 30 (2002) 237–243.